Observation and formation mechanism of 360° domain wall rings in synthetic anti-ferromagnets with interlayer chiral interactions

Miguel A. Cascales Sandoval,[1,2] (iD) A. Hierro-Rodríguez,[3,4,a)] (iD) S. Ruiz-Gómez,[5] (iD) L. Skoric,[6] (iD) C. Donnelly,[5] (iD) M. A. Niño,[7] (iD) E. Y. Vedmedenko,[8] (iD) D. McGrouther,[1] (iD) S. McVitie,[1] (iD) S. Flewett,[9] N. Jaouen,[10] (iD) M. Foerster,[7] (iD) and A. Fernández-Pacheco[1,2,11,a)] (iD)

AFFILIATIONS

[1]SUPA, School of Physics and Astronomy, University of Glasgow, Glasgow G12 8QQ, United Kingdom
[2]Institute of Applied Physics, TU Wien, Wiedner Hauptstraße 8-10, Vienna 1040, Austria
[3]Departamento de Física, Universidad de Oviedo, 33007 Oviedo, Spain
[4]CINN (CSIC-Universidad de Oviedo), 33940 El Entrego, Spain
[5]Max Planck Institute for Chemical Physics of Solids, 01187 Dresden, Germany
[6]University of Cambridge, Cambridge CB3 0HE, United Kingdom
[7]ALBA Synchrotron Light Facility, 08290 Cerdanyola del Vallés, Spain
[8]Department of Physics, University of Hamburg, Hamburg, Germany
[9]Instituto de Física, Pontificia Universidad Católica de Valparaíso, Avenida Universidad 330, Valparaíso, Chile
[10]SOLEIL Synchrotron, L'ormes des Merisiers, 91192 Gif-Sur-Yvette, Cedex, France
[11]Instituto de Nanociencia y Materiales de Aragón, CSIC-Universidad de Zaragoza, 50009 Zaragoza, Spain

[a)]Authors to whom correspondence should be addressed: hierroaurelio@uniovi.es and amalio.fernandez-pacheco@tuwien.ac.at

ABSTRACT

The interlayer Dzyaloshinskii–Moriya interaction (IL-DMI) chirally couples spins in different ferromagnetic layers of multilayer heterostructures. So far, samples with IL-DMI have been investigated utilizing magnetometry and magnetotransport techniques, where the interaction manifests as a tunable chiral exchange bias field. Here, we investigate the nanoscale configuration of the magnetization vector in a synthetic anti-ferromagnet (SAF) with IL-DMI, after applying demagnetizing field sequences. We add different global magnetic field offsets to the demagnetizing sequence in order to investigate the states that form when the IL-DMI exchange bias field is fully or partially compensated. For magnetic imaging and vector reconstruction of the remanent magnetic states, we utilize x-ray magnetic circular dichroism photoemission electron microscopy, evidencing the formation of 360° domain wall rings of typically 0.5–3.0 μm in diameter. These spin textures are only observed when the exchange bias field due to the IL-DMI is not perfectly compensated by the magnetic field offset. From a combination of micromagnetic simulations, magnetic charge distribution, and topology arguments, we conclude that a non-zero remanent effective field with components both parallel and perpendicular to the anisotropy axis of the SAF is necessary to observe the rings. This work shows how the exchange bias field due to IL-DMI can lead to complex metastable spin states during reversal, important for the development of future spintronic devices.

The interlayer Dzyaloshinskii–Moriya interaction (IL-DMI) is an interlayer-mediated antisymmetric exchange interaction observed in multilayer heterostructures, which promotes orthogonal coupling between spins in different magnetic layers.[1–4] This interaction contrasts with the well established intralayer DMI,[5,6] which chirally couples spins within the same magnetic layer. IL-DMI is a coupling mechanism that may find interesting applications in 3D nanomagnetism, as it provides the opportunity of inducing chiral magnetic states in a layer controlled by the magnetic state of another.

IL-DMI can be understood as an effective unidirectional magnetic field breaking the symmetry of the reversal process, leading to a chiral exchange bias.[2] This exchange bias field has been for instance utilized to achieve field free spin-orbit torque mediated deterministic switching of perpendicularly magnetized thin film systems,[7–11] as an alternative to exchange bias generated at ferromagnet/anti-ferromagnet interfaces. So far, samples with IL-DMI have been typically investigated with magnetometry and magnetotransport techniques, such as the magneto-optical Kerr effect (MOKE)[1] and anomalous Hall effect.[2,12,13]

Here, the remanent magnetic domain configurations present in a synthetic anti-ferromagnet (SAF) with chiral exchange coupling due to IL-DMI are investigated using x-ray magnetic circular dichroism photo-emission electron microscopy (XMCD-PEEM). The states imaged are obtained after performing a demagnetizing[14,15] process with different external field offsets added to the cycling sequence. By combining multiple XMCD-PEEM projections measured at different azimuthal angles, the magnetization vector is reconstructed, evidencing the formation of 360° domain wall (DW) rings. The IL-DMI is found to be key for the stability of these structures, as rings are only observed when the exchange bias IL-DMI field is not fully compensated by the external field offset. Experiments are complemented with micromagnetic simulations, which highlight the importance of the relative orientation of external and demagnetizing dipolar magnetic fields with the in plane anisotropy axis of the sample for the formation of the 360° DW rings.

The SAF structure under investigation consists of Si/Ta (4 nm)/Pt (10 nm)/Co (1 nm)/Pt (0.5 nm)/Ru (1 nm)/Pt (0.5 nm)/CoFeB (2 nm)/Pt (2 nm)/Ta (4 nm), deposited by sputtering. The Co layer has dominating strong perpendicular magnetic anisotropy (PMA) provided by the Pt at the interfaces (surface anisotropy $K_s = 1.2$ mJm^{-2})[1] i.e., it is a hard out-of plane (OOP) layer. In contrast, the CoFeB (Co: 60%, Fe: 20%, B: 20%) has been tailored to exhibit moderately low in-plane (IP) anisotropy, achieved by tuning its thickness slightly above the spin reorientation transition which takes place at 1.55 nm. The transition thickness occurs when the surface anisotropy ($K_s = 0.7$ mJm^{-2})[1] balances the thin film shape anisotropy, i.e., $K_{eff} = 2K_s/t - 0.5\mu_0 M_s^2 = 0$, with M_s being the saturation magnetization ($M_s^{CoFeB} = 1.2 \times 10^6$ Am^{-1}, $M_s^{Co} = 1.4 \times 10^6$ Am^{-1}). During deposition, a magnetic field of ∼100 mT was applied providing further IP anisotropy in the CoFeB layer along the field direction. This effect is negligible on the Co layer, due to dominating PMA. The Pt layers in between both ferromagnetic layers serve several purposes. They provide PMA to the ferromagnetic layers, high spin orbit coupling to enhance the DMI, and also damp the antiferromagnetic Ruderman–Kittel–Kasuya–Yosida (RKKY) interactions due to the Ru spacer. Lastly, the Ta seed layer provides an appropriate basis for the growth of the remaining layers, whereas the top Ta protects the sample from oxidation.

In this type of SAFs, a chiral exchange bias due to IL-DMI has been previously observed under measurement of minor IP hysteresis loops on which solely the CoFeB layer reverses while the Co stays fixed in the OOP direction. Upon reversal of the orientation of the Co layer, the exchange bias changes sign. The unidirectional nature of the effect is manifested by the IP angular dependence of the bias,[1] which shows opposite sign for the two possible directions parallel to the IP anisotropy easy axis (EA), and zero for the directions orthogonal to it. In particular for the sample investigated here, the magnitude of the

exchange bias field along the EA is 3.3 mT, compared with a coercivity of 4.0 mT, as evidenced by Figs. 2(c) and 2(d).

To investigate the effect of IL-DMI on the domain states forming in these samples, magnetic microscopy measurements were taken at CIRCE[16] beamline in ALBA Synchrotron, using XMCD-PEEM (see sketch in Fig. 1). In this setup, the azimuthal angle of the sample with respect to the x-rays can be modified in the full 360° angular range, while the incidence angle is fixed to 16° with respect to the surface plane, giving large sensitivity to IP components. Both circular polarization images are recorded and combined exploiting XMCD for magnetic contrast,[17–19] measured at both Fe and Co's L_3 absorption edges at each magnetic state. Prior to the experiments, 50 nm thick Pt$_x$C$_{1-x}$ squares and rectangles were deposited using focused electron beam induced deposition (FEBID) on top of the film, serving as non-magnetic references for equalizing both circular polarization images in order to properly compute the final XMCD image. The holder used for mounting the sample into the PEEM chamber has an embedded dipolar electromagnet,[16,20] giving the possibility of applying in-plane uniaxial magnetic fields ($\vec{B}_{ext}$). The nominal IP EA of the CoFeB ($\hat{x}$), given by the rectangle alignment mark's long axis, is mounted parallel to the electromagnet's axis after previously saturating the Co layer in one of the OOP directions.
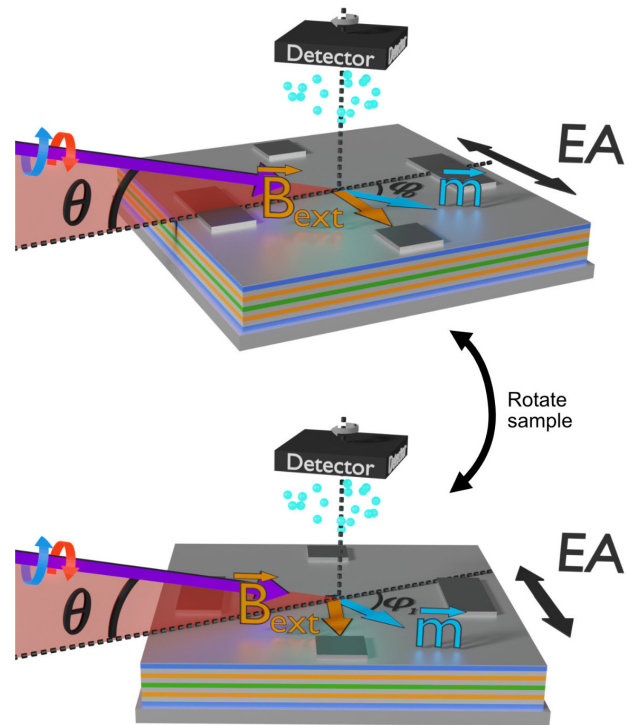
FIG. 1. Schematic of two different relative sample/x-ray beam orientations. φ_0 and φ_1 are the different relative angles between the x-ray beam (purple arrow) and the magnetization vector (blue arrow and $\vec{m}$ symbol) upon sample rotation about the axis normal to the substrate, θ is the incidence angle with respect to the surface plane of the x rays, the blue and red circular arrows denote both x-ray circular polarization eigenmodes, $\vec{B}_{ext}$ the external magnetic field direction provided by the dipolar electromagnet, the blue dots represent the emitted photo-electrons, and the double headed EA arrow represents the IP anisotropy axis of the CoFeB layer.
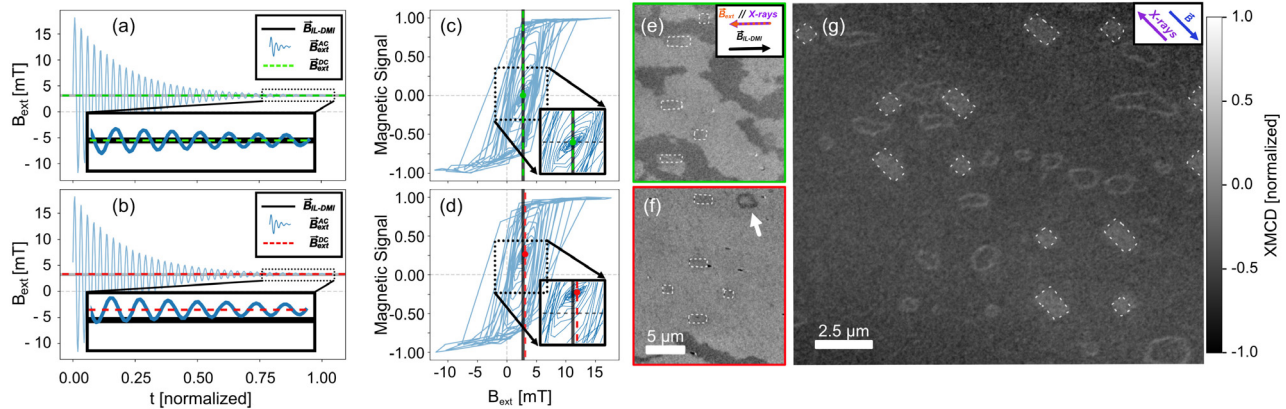
FIG. 2. (a) and (b) External field demagnetizing protocol, compensating either fully (a), or partially (b) the IL-DMI exchange bias field via a field offset ($B_x = 0$ and $B_x \neq 0$). (c) and (d) XRMS measurements taken with circular incident polarization during application of the demagnetization procedure, respectively, for the field sequences in (a) and (b). (e) and (f) XMCD-PEEM images measured at final green and red cases at Co's L_3 edge. The inset in (e) is common to (f), representing the external magnetic field, x-ray, and IL-DMI field directions. (g) XMCD-PEEM image taken at Co's L_3 edge after partially demagnetizing the CoFeB film and utilizing a larger FOV, evidencing the formation of a large number of rings. The inset here shows the direction of the x rays and the net effective field acting on the sample. The white dashed lines in (e), (f), and (g) denote the non-magnetic reference Pt_xC_{1-x} squares and rectangles.

In order to obtain a magnetically non-trivial remanent state, a demagnetization protocol, which consists of consecutively decreasing IP sinusoidal $\vec{B}_{ext}$ signals, is applied. $\vec{B}_{ext}$, thus, consists of an AC oscillating component ($\vec{B}_{ext}^{AC}$), and a DC or external field offset component ($\vec{B}_{ext}^{DC}$). The protocol is demonstrated in Fig. 2, where the magnetization is probed in a separate x-ray resonant magnetic scattering (XRMS) experiment, performed at SEXTANTS beamline in SOLEIL synchrotron. For this, XRMS hysteresis loops are taken where the specularly reflected signal is recorded, using field sequences where the IL-DMI exchange bias field ($\vec{B}_{IL-DMI}$) is either fully or partially compensated by $\vec{B}_{ext}^{DC}$. The x-ray beam spot used is 300 μm in diameter,[21] and the x-ray beam was set to 13° of incidence with respect to the sample plane, giving large sensitivity to the IP magnetization.[22]

Figures 2(c) and 2(d) show the XRMS hysteresis loops for the two demagnetizing sequences in Figs. 2(a) and 2(b). In the green (fully demagnetized case) shown in Fig. 2(c), $\vec{B}_{IL-DMI}$'s $\hat{x}$ component is fully compensated by $\vec{B}_{ext}$, i.e., $B_x = 0$, with $\vec{B} = \vec{B}_{ext} - \vec{B}_{IL-DMI}$, yielding final zero net magnetic signal. This state corresponds to the one observed via XMCD-PEEM in Fig. 2(e), where the area of black and white domains within the field of view (FOV) is indeed approximately equal. The situation is different for the red (partially demagnetized case) shown in Fig. 2(d), where $\vec{B}_{IL-DMI}$'s $\hat{x}$ component is not fully compensated ($B_x \neq 0$), reaching a final state with non-zero net magnetic signal. This agrees with the corresponding PEEM experiment shown in Fig. 2(f), where there is a clear dominating magnetic configuration aligned with $\vec{B}_{ext}$. In the partially demagnetized case, a number of ring-like magnetic textures (0.5–3.0 μm in diameter) are frequently observed by PEEM, for instance, the one marked by the white arrow in Fig. 2(f). The emergence of a large number of rings is found in partially demagnetized states as the one in Fig. 2(g), where an area with a larger field of view is shown. All the images shown here are taken at the Co L_3 edge and refer to states forming on the CoFeB layer, since the magnetic features are identical at both Fe and Co edges, with Co showing a

significantly better signal-to-noise ratio due to the stoichiometry of the CoFeB layer (see the supplementary material).

In the experiments, other demagnetizing sequences with offset fields of different magnitude were performed. The maximum offset investigated was 0.8 mT larger than the one that perfectly compensates the exchange bias, i.e., $B_x = 0.8$ mT. We observe a decrease in the number of rings as the offset field increases, with a few of them still present at this maximum offset.

To understand better the magnetic configuration of these spin textures, vector imaging of one of the rings is performed by measuring several x-ray beam/sample projections. For this, the sample is rotated in the PEEM chamber with respect to the x-ray direction, as shown in Fig. 1. XMCD images are obtained for a total of eight azimuthal angles, see Fig. 3 (a). The images have been previously rotated and aligned with respect to each other in order to have the same spatial orientation, following a similar procedure to the one described in.[23] Additionally, deformations in different projection images are corrected by an algorithm, which makes use of a combination of image registration techniques, using the Pt_xC_{1-x} marker's geometrical shape as reference landmarks. These deformations arise from the fact that the used PEEM microscope does not inherently present circular symmetry. Some of the electron optical elements, in particular, the 120° beam splitter, typically introduce image distortions, which become relevant when overlaying images for different sample orientations.

The spatially resolved normalized magnetization vector ($\vec{m}$) is then reconstructed,[23–29] by performing a pixel-by-pixel least squares fitting of the XMCD profile (given by $\vec{k} \cdot \vec{m}$, with $\vec{k}$ being the incident x-ray wave-vector) as a function of the azimuthal rotation angle. The resulting vector directions of $\vec{m}$ are shown in the central image of Fig. 3(a). The line profiles in Fig. 3(b) evidence the presence of 360° DWs separating the outer and inner domains, whose orientation is the same, and the direction of $\vec{m}$ within them is the result of the EA and $\vec{B}$ directions. In the reconstruction, great precision is achieved in the determination of the IP components due to the grazing incidence of the x-rays, which on the other hand reduces the sensitivity to OOP components. Furthermore, the magnetic signal decreases in areas
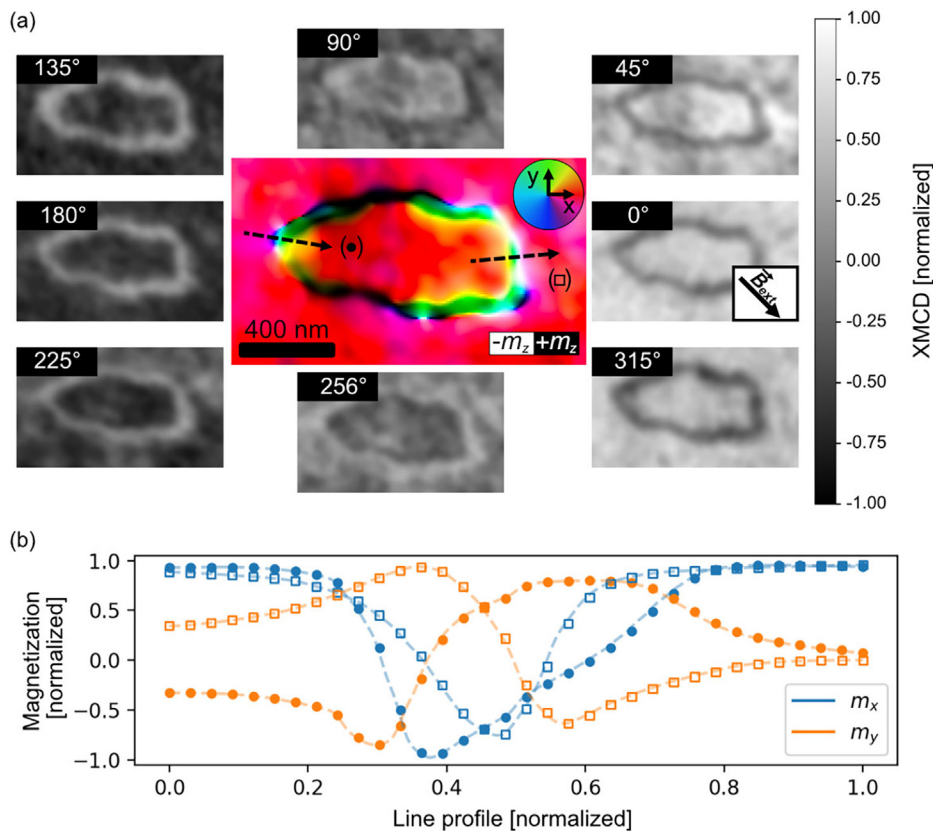
FIG. 3. (a) XMCD-PEEM based vector reconstruction of the magnetization of a 360° DW ring using eight projections. Gray-scale images correspond to the 8 XMCD-PEEM projections taken at different azimuthal x-ray beam/sample relative angles. The angle of each projection is given with respect to the x-axis indicated in the central figure. The applied external magnetic field direction is given by the inset arrow of the 0° projection. The central color-map represents the spatially resolved magnetic vector configuration, utilizing the hsl colormap for the IP directions, and black and white for the OOP directions. (b) IP components of $\vec{m}$ along the profiles given by the dashed arrows overlayed on the central color plot, evidencing 360° DW.

where the magnetization changes over small spatial lengthscales in comparison with the microscope's resolution, giving a larger uncertainty in the domain walls' OOP components.

360° DW rings have been previously observed in individual ferromagnetic Permalloy thin film layers,[30] in multilayered heterostructures,[31–33] in exchanged biased films,[15,34,35] and in magnetic tunnel junctions.[36] The role of Bloch lines,[31] DW splitting,[32] and dispersion in anisotropy[15] have been proposed as mechanisms for explaining their formation.

In order to determine the dependence between the stability of 360° DW rings and the IL-DMI effective field, focus is first set on their topology and magnetic charge distribution. For this, the simplified sketch of the vector reconstructed configuration shown in Fig. 4(a) is used, assuming a fully IP texture. The figure shows an elongated, 360° DW ring with the EA along $\vec{x}$. A 1D 360° DW is a topologically non-trivial structure, having been sometimes denominated 1D skyrmions in the literature.[37] However, when these DW form a ring structure as the one shown here, the net winding number computed along a line profile diametrically crossing the whole ring is zero due to the opposite chirality of the two encountered 360° DW. Therefore, a 360° DW ring as a whole is topologically trivial, which means that it can be continuously deformed into a single domain state.

Additionally, the elongation observed for the ring textures along the EA is expected based on magnetostatics arguments, *i.e.*, Néel walls prefer to align parallel to the EA rather than perpendicular[38] to it. Furthermore, the magnetic charge distribution along the ring structure is anisotropic,

as evidenced by the "+" and "−" in the figure. For both (top and bottom) walls parallel to the EA, the two 180° DW forming the 360° DW repel each other, which in combination with the ferromagnetic exchange promote the growth of the annular domain (cyan). In the absence of a net magnetic field, this magnetic texture would expand and relax into broader domains separated by consecutive 180° DW.[39] This contrasts with the (left and right) DW orthogonal to the anisotropy axis, where the demagnetizing field arising from the charge distribution now makes the two consecutive 180° DW attract each other, opposing the expansion of the annular domain promoted by ferromagnetic exchange. The competition of these interactions dictates the stability of the vertical 360° DW component at zero field.[39] Thus, for the overall 360° DW ring texture to remain stable, a net non-zero $\vec{B}$ field along the easy axis is required to compress from both inner and outer parts, preventing it from relaxing and expanding into broader domains, i.e., two consecutive domains separated by 180° DWs. Additionally, this field prevents the unwinding of the inner domain due to it being topologically trivial. This agrees well with previous observations of 360° DW rings in systems with exchange bias,[15,34,35] since the field sequences used there do not add field offsets, resulting in net non-zero fields at remanence.

Finally, we focus on investigating the mechanism behind the nucleation of the rings using micromagnetic simulations. For this, solely a single IP thin film is modeled representing the CoFeB layer of the SAF, whose simulation parameters are summarized in Table I. As in experiments, $\vec{B}_{IL-DMI}$ is parallel to the EA (horizontal $\vec{x}$ direction), and it is modeled through the effective field $\vec{B}$. In these simulations, we
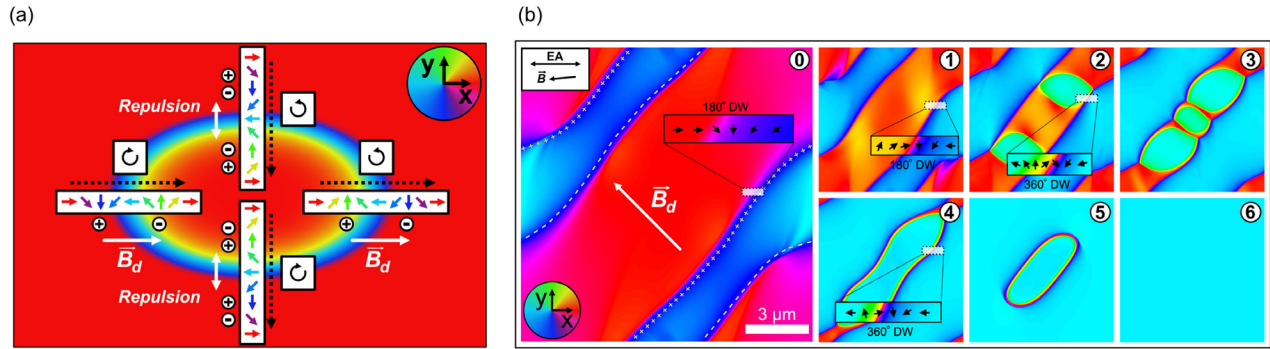
FIG. 4. (a) Simplified sketch of a 360° DW ring as the one obtained in the reconstruction shown in Fig. 3, where the magnetization winding sense at four different locations is illustrated by the colored arrows. The rotating arrows denote the sense of rotation of magnetic spins along the dashed line arrows. (b) Dynamical evolution (numbered states) of the simulation space to study the formation of 360° DW rings with IP magnetization vector directions given by the hsl colormap. EA and magnetic field $\vec{B}$ directions are indicated by the inset arrows in state 0. In state (0), $\vec{B}_d$ represents the demagnetizing field arising from the magnetic charges "+" and "−," which is non-homogeneous and becomes stronger as the domain walls get closer to each other (subsequent states). The time for each state is given relatively to state (0); $t_1 = 0.10$ ns, $t_2 = 0.22$ ns, $t_3 = 0.42$ ns, $t_4 = 0.66$ ns, $t_5 = 1.90$ ns, and $t_6 = 3.40$ ns.

do not include additional effects related to the interaction between Co and CoFeB layers. In particular, the magnetostatic interaction in between the two layers is not considered. In the following, our simulations show a clear mechanism for the formation of the rings despite this approximation.

In order to model the formation process via micromagnetic simulations, the first step consists of obtaining a magnetic configuration formed by multiple domains, resembling an intermediate state during the demagnetizing protocol. For this, the simulation starts from a fully saturated $+m_x$ configuration. Then, a $\vec{B}$ field of increasing magnitude is applied along $-\hat{x}$ with a small $-\hat{y}$ component (5° with respect to $+\hat{x}$), which represents a misalignment between $\vec{B}_{ext}$ and the EA. A circular defect of 0.8 μm radius and with 20% anisotropy value of the layer is included to trigger the nucleation of domains (cyan). Once $\vec{B}$ reaches the switching field magnitude, the system is allowed to evolve dynamically, eventually reaching the state shown in [Fig. 4(b), state (0)]. All 180° DWs in the simulation space have a $-m_y$ component set by B_y,[14] resulting in the magnetic charge distribution, once again represented by the "+" and "−" signs.

As DW of opposite charge get closer promoted by the growth of the inverted domain, the intensity of the demagnetizing field ($\vec{B}_d$)

TABLE I. Parameters for the micromagnetic simulation. Values for parameters were, respectively, found at α,[40] M_S,[1] A_{exc},[41] and K.[1]

Parameter	Value
Cells (x, y, z)	$3072 \times 3072 \times 1$
Cell size (x, y, z)	$4.5 \times 4.5 \times 5.0$ (nm)
α	0.02
M_S	1.2×10^6 (A/m)
A_{exc}	20 (pJ/m)
K	1.8×10^3 (J/m^3)
Defect size	0.8 (μm)
Defect anisotropy	3.6×10^2 (J/m^3)
Periodic boundary conditions	16×16 (repetitions)

associated to the magnetic charges begins to increase [Fig. 4(b), state (1)]. The varying $\vec{B}_d$ in combination with the constant $\vec{B}$ eventually reaches the sufficient field magnitude for overcoming the anisotropy dominated nucleation field, as a consequence locally inverting the magnetization. This allows for the formation of a new pair of 180° DWs during the reversal, with their core magnetization pointing along $+m_y$, given that the $\hat{y}$ component of $\vec{B}_d$ in this case is opposite and larger in magnitude than the original set by $\vec{B}$, i.e., $B_{d_y} > -B_y$. This is exemplified in the crop shown in [Fig. 4(b), state (2)]; the new 180° DW forms next to the original →↓← from [Fig. 4(b), state (1)], resulting in a 360° DW with ←↑→↓← configuration. Thus, for the formation of 360° DW and the forthcoming rings, it is key for the $\hat{y}$ component of $\vec{B}_d$ to be opposite in sign and greater in magnitude than B_y. In the hypothetical case where either $\vec{B}$ and/or $\vec{B}_d$ were purely along $\hat{x}$, it would not have lead to the formation of the rings, as the existence of non-zero transverse field components is crucial.

From this point on, a ring is finally formed after the red domains shrink due to the opposing $\vec{B}$ [Fig. 4(b), states (3)–(5)]. The key role of an alternating B_y field [Fig. 4(b), states (0)–(1)] for the formation of 360° DW rings in a system with m_x domains is similar to previous works in nanowires with injection pads,[14] where 360° DW were stabilized via the application of alternating external magnetic fields. Here, instead, the net magnetic field is dominated by $\vec{B}_{ext}$ or $\vec{B}_d$, for different steps of formation.

In this ideal simulation space, the ring eventually annihilates [Fig. 4(b), state (6)], in contrast with the experimental results where rings remain stable. This can be readily explained due to the presence of pinning sites, defects, and imperfections in the real sample that locally alter the magnetic energy landscape, leading to their meta-stability.[42]

The mechanism for the formation and stabilization of rings described here is applicable to a single film subject to a demagnetizing sequence with a nonzero constant offset field. This type of procedure is more likely to happen in films with an intrinsic bias field, which explains the larger number of works reporting the observance of rings in exchanged bias bilayers.

In conclusion, we have observed 360° DW rings via XMCD-PEEM magnetic vector reconstruction, forming in a SAF exhibiting exchange bias due to IL-DMI. These textures are observed at remanence after applying IP demagnetizing field sequences where a global

offset in field is added. A combination of XMCD-PEEM and XRMS shows how the rings are only found when the field offset does not perfectly compensate for the IL-DMI exchange bias field present in the SAF. We propose a mechanism for the formation and stability of the rings, based on analyzing their magnetic charge distribution and topology, in combination with micromagnetic simulations. First, a non-zero net IP field parallel to the easy axis, result of external and IL-DMI fields, is key for their stability at remanence. This net field in combination with pinning sites prevents their relaxation and annihilation due to their trivial topology. Secondly, a non-zero component of the net field perpendicular to the easy axis is required for their formation. This component sets the initial direction of two 180° walls at the start of the reversal process, which subsequently combine with two other 180° walls that form afterward. The wall component of this second set of 180° walls is opposite to the original ones, set by the strong demagnetizing field in between domains that dominate as these become closer to each other. The combination of the two sets of consecutive 180° walls results in two 360° walls of opposite chirality, leading to a 360° wall ring. A deep understanding of the effect of IL-DMI on the magnetic reversal process and domain structure of SAFs is crucial for the potential exploitation of this effect in spintronic devices.

See the supplementary material for comparison between XMCD-PEEM images taken at Co and Fe edges (Fig. S1), evidencing identical magnetic textures in both cases.

AUTHOR DECLARATIONS
Conflict of Interest

The author have no conflicts to disclose.

Author Contributions

Miguel A. Cascales Sandoval: Conceptualization (lead); Data curation (lead); Formal analysis (lead); Investigation (lead); Methodology (lead); Software (lead); Visualization (lead); Writing – original draft (lead); Writing – review & editing (equal). **Aurelio Hierro-Rodríguez:** Conceptualization (equal); Data curation (equal); Formal analysis (equal); Investigation (equal); Methodology (equal); Supervision (equal); Writing – original draft (equal); Writing – review & editing (equal). **Sandra Ruiz-Gómez:** Data curation (lead); Investigation (equal); Writing – review & editing (equal). **Luka Skoric:** Investigation (equal); Software (supporting); Writing – review & editing (equal). **Claire Donnelly:** Investigation (equal); Writing – review & editing (equal). **Miguel Angel Niño:** Data curation (equal); Investigation (equal); Writing – review & editing (equal). **Elena Vedmedenko:** Investigation (equal); Writing – review & editing (equal). **Damien McGrouther:** Investigation (equal); Writing – review & editing (equal). **Stephen McVitie:** Investigation (equal); Writing – review & editing (equal). **Samuel Flewett:** Investigation (equal); Writing – review & editing (equal). **Nicolas Jaouen:** Conceptualization (equal); Investigation (equal); Writing – review & editing (equal). **Michael Foerster:** Conceptualization (equal); Data curation (equal); Formal analysis (equal); Investigation (equal); Writing – original draft (supporting); Writing – review & editing (equal). **Amalio Fernández-Pacheco:** Conceptualization (equal); Funding acquisition (equal); Investigation (equal); Methodology (equal); Project administration (equal); Resources (equal); Supervision (equal); Writing – original draft (equal); Writing – review & editing (equal).

DATA AVAILABILITY

The data utilized to generate the figures shown in the text can be found at the Enlighten repository of the University of Glasgow: https://doi.org/10.5525/gla.researchdata.1511.

REFERENCES

[1]A. Fernández-Pacheco, E. Vedmedenko, F. Ummelen, R. Mansell, D. Petit, and R. P. Cowburn, "Symmetry-breaking interlayer Dzyaloshinskii–Moriya interactions in synthetic antiferromagnets," Nat. Mater. **18**, 679–684 (2019).

[2]D.-S. Han, K. Lee, J.-P. Hanke, Y. Mokrousov, K.-W. Kim, W. Yoo, Y. L. Van Hees, T.-W. Kim, R. Lavrijsen, C.-Y. You, et al., "Long-range chiral exchange interaction in synthetic antiferromagnets," Nat. Mater. **18**, 703–708 (2019).

[3]E. Y. Vedmedenko, P. Riego, J. A. Arregi, and A. Berger, "Interlayer Dzyaloshinskii-Moriya interactions," Phys. Rev. Lett. **122**, 257202 (2019).

[4]C. O. Avci, C.-H. Lambert, G. Sala, and P. Gambardella, "Chiral coupling between magnetic layers with orthogonal magnetization," Phys. Rev. Lett. **127**, 167202 (2021).

[5]S. Tacchi, R. Troncoso, M. Ahlberg, G. Gubbiotti, M. Madami, J. Åkerman, and P. Landeros, "Interfacial Dzyaloshinskii-Moriya interaction in Pt/CoFeB films: Effect of the heavy-metal thickness," Phys. Rev. Lett. **118**, 147201 (2017).

[6]S. Xia, S. Zhang, Z. Luan, L. Zhou, J. Liang, G. Liu, B. Yang, H. Yang, R. Liu, and D. Wu, "Interfacial Dzyaloshinskii-Moriya interaction between ferromagnetic insulator and heavy metal," Appl. Phys. Lett. **116**, 052404 (2020).

[7]Y.-H. Huang, C.-C. Huang, W.-B. Liao, T.-Y. Chen, and C.-F. Pai, "Growth-dependent interlayer chiral exchange and field-free switching," Phys. Rev. Appl. **18**, 034046 (2022).

[8]Y.-C. Lau, D. Betto, K. Rode, J. Coey, and P. Stamenov, "Spin–orbit torque switching without an external field using interlayer exchange coupling," Nat. Nanotechnol. **11**, 758–762 (2016).

[9]W. He, C. Wan, C. Zheng, Y. Wang, X. Wang, T. Ma, Y. Wang, C. Guo, X. Luo, M. Stebliy, et al., "Field-free spin-orbit torque switching enabled by interlayer Dzyaloshinskii-Moriya interaction," arXiv:2205.06706 (2022).

[10]Z. Wang, P. Li, Y. Yao, Y. L. Van Hees, C. F. Schippers, R. Lavrijsen, A. Fert, W. Zhao, and B. Koopmans, "Field-free spin orbit torque switching of synthetic

antiferromagnet through interlayer Dzyaloshinskii-Moriya interaction," arXiv:2205.04740 (2022).

[11] Z. A. Bekele, X. Lan, K. Meng, and X. Liu, "Enhanced field-free current-induced magnetization switching by interlayer exchange coupling with insulating spacer layer," J. Appl. Phys. **127**, 113902 (2020).

[12] K. Wang, L. Qian, S.-C. Ying, and G. Xiao, "Spin-orbit torque switching of chiral magnetization across a synthetic antiferromagnet," Commun. Phys. **4**, 10 (2021).

[13] F. Kammerbauer, W.-Y. Choi, F. Freimuth, K. Lee, R. Frömter, D.-S. Han, H. J. Swagten, Y. Mokrousov, and M. Kläui, "Controlling 3D spin textures by manipulating sign and amplitude of interlayer DMI with electrical current," arXiv:2209.01450 (2022).

[14] Y. Jang, S. R. Bowden, M. Mascaro, J. Unguris, and C. Ross, "Formation and structure of 360 and 540 degree domain walls in thin magnetic stripes," Appl. Phys. Lett. **100**, 062407 (2012).

[15] J. Dean, A. Kohn, A. Kovacs, A. Zeltser, M. Carey, G. Hrkac, D. Allwood, and T. Schrefl, "The formation mechanism of 360 domain walls in exchange-biased polycrystalline ferromagnetic films," J. Appl. Phys. **110**, 073901 (2011).

[16] L. Aballe, M. Foerster, E. Pellegrin, J. Nicolas, and S. Ferrer, "The ALBA spectroscopic LEEM-PEEM experimental station: layout and performance," J. Synchrotron Radiat. **22**, 745–752 (2015).

[17] J. Stöhr and H. C. Siegmann, "Magnetism," in *Solid-State Sciences* (Springer, Berlin, Heidelberg, 2006), Vol. 5, p. 236.

[18] E. Beaurepaire, F. Scheurer, G. Krill, and J.-P. Kappler, *Magnetism and synchrotron radiation* (Springer, 2001), Vol. 34.

[19] T. Yokoyama, T. Nakagawa, and Y. Takagi, "Magnetic circular dichroism for surface and thin film magnetism: Measurement techniques and surface chemical applications," Int. Rev. Phys. Chem. **27**, 449–505 (2008).

[20] M. Foerster, J. Prat, V. Massana, N. Gonzalez, A. Fontsere, B. Molas, O. Matilla, E. Pellegrin, and L. Aballe, "Custom sample environments at the ALBA XPEEM," Ultramicroscopy **171**, 63–69 (2016).

[21] N. Jaouen, J.-M. Tonnerre, G. Kapoujian, P. Taunier, J.-P. Roux, D. Raoux, and F. Sirotti, "An apparatus for temperature-dependent soft x-ray resonant magnetic scattering," J. Synchrotron Radiat. **11**, 353–357 (2004).

[22] E. Jal, "Réflectivité magnétique résonante de rayons X mous: Une sonde de la distribution d'aimantation complexe au sein de films minces," Ph.D. thesis (Grenoble, 2013).

[23] L. Le Guyader, A. Kleibert, A. F. Rodríguez, S. El Moussaoui, A. Balan, M. Buzzi, J. Raabe, and F. Nolting, "Studying nanomagnets and magnetic heterostructures with X-ray PEEM at the Swiss Light Source," J. Electron Spectrosc. Relat. Phenom. **185**, 371–380 (2012).

[24] S. Ruiz-Gómez, L. Pérez, A. Mascaraque, A. Quesada, P. Prieto, I. Palacio, L. Martín-García, M. Foerster, L. Aballe, and J. de la Figuera, "Geometrically defined spin structures in ultrathin Fe_3O_4 with bulk like magnetic properties," Nanoscale **10**, 5566–5573 (2018).

[25] M. Ghidini, F. Maccherozzi, S. S. Dhesi, and N. D. Mathur, "XPEEM and MFM imaging of ferroic materials," Adv. Electron. Mater. **8**, 2200162 (2022).

[26] A. Scholl, H. Ohldag, F. Nolting, J. Stöhr, and H. A. Padmore, "X-ray photoemission electron microscopy, a tool for the investigation of complex magnetic structures," Rev. Sci. Instrum. **73**, 1362–1366 (2002).

[27] R. Chopdekar, J. Heidler, C. Piamonteze, Y. Takamura, A. Scholl, S. Rusponi, H. Brune, L. Heyderman, and F. Nolting, "Strain-dependent magnetic configurations in manganite-titanate heterostructures probed with soft x-ray techniques," Eur. Phys. J. B **86**, 241 (2013).

[28] F. P. Chmiel, N. Waterfield Price, R. D. Johnson, A. D. Lamirand, J. Schad, G. van der Laan, D. T. Harris, J. Irwin, M. S. Rzchowski, C.-B. Eom, *et al.*, "Observation of magnetic vortex pairs at room temperature in a planar α-Fe_2O_3/Co heterostructure," Nat. Mater. **17**, 581–585 (2018).

[29] E. Digernes, S. D. Slöetjes, A. Strùmberg, A. D. Bang, F. K. Olsen, E. Arenholz, R. V. Chopdekar, J. K. Grepstad, and E. Folven, "Direct imaging of long-range ferromagnetic and antiferromagnetic order in a dipolar metamaterial," Phys. Rev. Res. **2**, 013222 (2020).

[30] D. Smith and K. Harte, "Noncoherent switching in permalloy films," J. Appl. Phys. **33**, 1399–1413 (1962).

[31] L. Heyderman, H. Niedoba, H. Gupta, and I. Puchalska, "360 and 0 walls in multilayer permalloy films," J. Magn. Magn. Mater. **96**, 125–136 (1991).

[32] L. Heyderman, J. Chapman, and S. Parkin, "TEM investigation of the magnetisation processes in exchange coupled multilayer films," J. Magn. Magn. Mater. **138**, 344–354 (1994).

[33] X. Portier and A. Petford-Long, "The formation of 360 domain walls in magnetic tunnel junction elements," Appl. Phys. Lett. **76**, 754–756 (2000).

[34] R. Schafer, A. Hubert, and S. Parkin, "Domain and domain wall observations in sputtered exchange-biased wedges," IEEE Trans. Magn. **29**, 2738–2740 (1993).

[35] H. S. Cho, C. Hou, M. Sun, and H. Fujiwara, "Characteristics of 360-domain walls observed by magnetic force microscope in exchange-biased NiFe films," J. Appl. Phys. **85**, 5160–5162 (1999).

[36] M. Gillies, J. Chapman, and J. Kools, "Magnetization reversal mechanisms in NiFe/Cu/NiFe/FeMn spin-valve structures," J. Appl. Phys. **78**, 5554–5562 (1995).

[37] R. Cheng, M. Li, A. Sapkota, A. Rai, A. Pokhrel, T. Mewes, C. Mewes, D. Xiao, M. De Graef, and V. Sokalski, "Magnetic domain wall skyrmions," Phys. Rev. B **99**, 184412 (2019).

[38] A. Hubert and R. Schäfer, *Magnetic Domains: The Analysis of Magnetic Microstructures* (Springer Science & Business Media, 2008).

[39] C. Muratov and V. Osipov, "Theory of 360 domain walls in thin ferromagnetic films," J. Appl. Phys. **104**, 053908 (2008).

[40] H. Głowiński, A. Żywczak, J. Wrona, A. Krysztofik, I. Gościańska, T. Stobiecki, and J. Dubowik, "CoFeB/MgO/CoFeB structures with orthogonal easy axes: perpendicular anisotropy and damping," J. Phys. **29**, 485803 (2017).

[41] T. Devolder, J.-V. Kim, L. Nistor, R. Sousa, B. Rodmacq, and B. Diény, "Exchange stiffness in ultrathin perpendicularly magnetized CoFeB layers determined using the spectroscopy of electrically excited spin waves," J. Appl. Phys. **120**, 183902 (2016).

[42] J. M. Coey, *Magnetism and Magnetic Materials* (Cambridge University Press, 2010).

14 February 2024 13:27:46